Article

Targeting Apollo-NADP$^+$ to Image NADPH Generation in Pancreatic Beta-Cell Organelles

Huntley H. Chang,[⊥] Alex M. Bennett,[⊥] William D. Cameron, Eric Floro, Aaron Au, Christopher M. McFaul, Christopher M. Yip, and Jonathan V. Rocheleau*

Cite This: ACS Sens. 2022, 7, 3308−3317

Read Online

ACCESS | 📊 Metrics & More | 📖 Article Recommendations | 🆘 Supporting Information

ABSTRACT: NADPH/NADP$^+$ redox state supports numerous reactions related to cell growth and survival; yet the full impact is difficult to appreciate due to organelle compartmentalization of NADPH and NADP$^+$. To study glucose-stimulated NADPH production in pancreatic beta-cell organelles, we targeted the Apollo-NADP$^+$ sensor by first selecting the most pH-stable version of the single-color sensor. We subsequently targeted mTurquoise2-Apollo-NADP$^+$ to various organelles and confirmed activity in the cytoplasm, mitochondrial matrix, nucleus, and peroxisome. Finally, we measured the glucose- and glutamine-stimulated NADPH responses by single- and dual-color imaging of the targeted sensors. Overall, we developed multiple organelle-targeted Apollo-NADP$^+$ sensors to reveal the prominent role of beta-cell mitochondria in determining NADPH production in the cytoplasm, nucleus, and peroxisome.
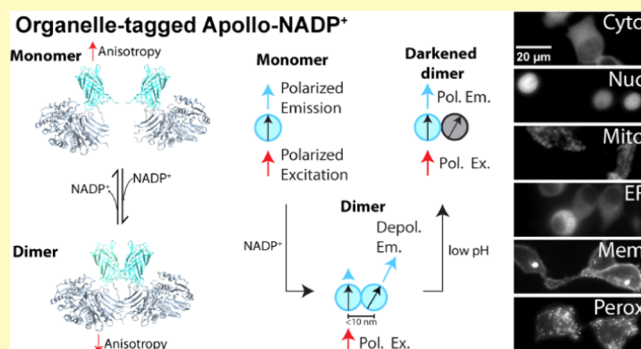
NADPH/NADP$^+$ redox state provides electrons to biosynthetic reactions required for cell growth and proliferation and to recharging antioxidants required for survival.[1] NADPH/NADP$^+$ redox state is thought to be compartmentalized due to a lack of known NADPH or NADP$^+$ membrane transporters and the existence of organelle-specific enzymes for NADP$^+$ biosynthesis and reduction.[1,2] Significant compartmentalization could create disparate impacts on organelle-specific anabolism and antioxidation. Our goal was to target a sensor we previously developed, Apollo-NADP$^+$, to organelles to measure organelle-specific NADPH compartmentalization.

Pancreatic beta-cells metabolically respond to glucose to stimulate insulin secretion. This response includes a rise in the NADPH/NADP$^+$ ratio. Pancreatic beta-cells show limited glucose-6-phosphate dehydrogenase (G6PD) activity[3] and thus rely on cytoplasmic malic enzyme (ME)[4−6] and/or isocitrate dehydrogenase (IDH1)[7] activity driven by metabolite efflux from the mitochondria. Mitochondria generate their own NADPH using NADP$^+$-dependent isocitrate dehydrogenase (IDH2) and nicotinamide nucleotide transhydrogenase (NNT)[8] with previous work suggesting NNT dominates the glucose-stimulated response.[9−12] Thus, we aimed to measure the metabolic routes of beta-cell glucose-stimulated NADPH production and the extent of redox crosstalk between organelles.

Several genetically encoded NADPH/NADP$^+$ redox state sensors are available, including the NADPH-sensitive iNAP sensor[13,14] and the NADP$^+$-sensitive NADPsor,[15] NADP-Snifit,[16] and Apollo-NADP$^+$ sensors.[17] Apollo-NADP$^+$ sensors are based on enzymatically inactive glucose-6-phosphate dehydrogenase (G6PD) and homo-dimerize upon binding free NADP$^+$ with a K_D of ∼3 μM.[17] This sensitivity is similar to the iNAP sensor family.[13] Tagged with a single fluorescent protein, Apollo-NADP$^+$ sensors uniquely respond through changes in steady-state fluorescence anisotropy due to FRET between homologous fluorescent proteins (homoFRET). A stimulated rise in steady-state fluorescence anisotropy (e.g., glucose-stimulated) is evidence of NADP$^+$ reduction to NADPH (i.e., NADPH production) with the caveat that slower biosynthesis/degradation of total NADP(H) could also impact the response. Importantly, anisotropy sensors consume less spectral bandwidth than conventional ratiometric sensors and can be swapped to distinct colors (i.e., they are spectrally tuneable), both of which facilitate multiparameter imaging.[17−19]

In this study, we target Apollo-NADP$^+$ to various organelle compartments. We subsequently use simultaneous two-color imaging to show a dominant role of mitochondrial NADPH generation in setting the glucose-stimulated responses in the cytoplasm, nucleus, and peroxisome.

■ MATERIALS AND METHODS

Molecular Biology of Sensor Targeting. We cloned mCerulean1 and mVenus-tagged Apollo-NADP$^+$ into the NheI/XhoI sites of pcDNA3.1(+) (Invitrogen, Burlington, Canada). The mTurqoise2 and mCerulean3 versions were subsequently created by exchanging the fluorescent protein using the AgeI/Xho1 sites. Organelle targeting sequences were introduced into the mTurquoise2 version of Apollo-NADP$^+$. Smaller tags were introduced using cloning primers, including the nuclear targeting sequence of SV40 T-antigen "PKKKRK" into the N-terminus,[20] the peroxisome targeting sequence −SKL into the C-terminus,[21] and the ER retention KDEL sequence into the C-terminus. Larger tags were cloned into the NheI and BamHI/HindIII sites, on the N-terminus of Apollo-NADP$^+$. We cloned in the mitochondrial matrix targeting sequence from pKillerRed-dMito (a gift from Peter Kim, SickKids Hospital, Toronto) to get four copies of the Cox8 mitochondrial targeting sequence. The membrane targeting sequence of neuromodulin was cloned from pEYFP-Mem, and the ER targeting sequence of calreticulin was cloned from pECFP-ER (Clontech, San Jose, CA). All constructs were confirmed by sequencing. All plasmid amplification was performed using 5-alpha competent Escherichia coli (NEB, Ipswich, MA, C2987I). The organelle-targeted sensors are deposited on Addgene.

Cells and Cell Culture. INS-1E (obtained from lab of Michael B. Wheeler, RRID: CVCL_0351) and AD293 (Agilent, Santa Clara, CA, #240085) cells were cultured in RPMI and DMEM media, respectively, under humidified 5% CO$_2$ at 37 °C. For imaging, the cells were plated into no. 1.5 glass-bottom dishes (MatTek Corporation, Ashland, MA) and transfected the next day (0.5−1.0 μg/dish/plasmid) using Poly-Jet reagent (for AD293s) (SignaGen, Frederick, MD) or Lipofectamine 3000 (for INS-1Es) (Invitrogen, Burlington, Canada) and incubated for 24 h. The media was replaced with fresh media, and the cells were left to recover for a further 24 h prior to imaging.

Clamping the Intracellular pH of Live Cells. Cytoplasmic pH was assessed using the Intracellular pH Calibration Buffer Kit (Invitrogen, Burlington, Canada). Cytoplasmic pH was varied as described previously.[22] Cell loading solutions were prepared to the specified pH using 10 μM valinomycin and 10 μM nigericin and the buffer solutions provided in the kit. Cells were incubated in the specified pH solutions for 5 min to allow for equilibration of intracellular and extracellular pH levels before imaging.

Islet Isolation, Dispersion, and Transduction. Animal procedures were approved by the Animal Care Committee of the University Health Network, Toronto ON, Canada, in accordance with the policies of the Canadian Council on Animal Care (Animal Use Protocol #1531). Pancreatic islets were isolated from 8- to 12-week-old C57Bl/6J (Jackson Lab, Bar Harbor, ME, RRID: IMSR_JAX:000664) male mice by collagenase digestion (Roche Applied Science).[23] Isolated islets were transferred into an Eppendorf tube (1.5 mL) containing 50 μL of RPMI islet media and 50 μL of trypsin/ethylenediamine tetraacetic acid (EDTA), immersed in a water bath at 37 °C, and shaken gently by hand for 12 min. The dissociated islet slurry was topped up to 1 mL total volume with RPMI islet media. Glass-bottom plates (48-well) were coated with poly-D-lysine hydrobromide (Sigma-Aldrich, Product #P6407) for 1 h at 37 °C to promote cell adhesion. The dispersed cells were transduced with adenovirus (24 h at 1:10 dilution or 2×10^7 IFU/mL).[24] Viral titers were measured using the Adeno-X rapid titer kit (Clontech) following manufacturer protocol.

Cellular Imaging. All imaging was done in BMHH imaging buffer (125 mM NaCl, 5.7 mM KCl, 2.5 mM CaCl$_2$, 1.2 mM MgCl$_2$, 0.1% bovine serum albumin (BSA), and 10 mM 4-(2-hydroxyethyl)-1-

piperazineethanesulfonic acid (HEPES) at pH 7.4). Single-color two-photon fluorescence anisotropy imaging was performed using an LSM710 confocal microscope (Zeiss, Toronto, Canada) equipped with a tunable Chameleon laser (Coherent, Santa Clara, CA). Images were collected using 840 or 950 nm excitation and a 63×/1.4 NA oil-immersion objective. Fluorescence was collected using the non-descanned binary GaAsP BiG (Zeiss, Toronto, Canada) detector with a custom-built filter cube containing an infrared-light-blocked Cerulean (ET480/40M-2P) or Venus (ET525/50M-2P) emission bandpass filter (Chroma, Bellows Falls, VT), polarizing beam-splitter (Edmund Optics, Barrington, NJ), and clean-up polarizers (Chroma, Bellows Falls, VT). For the purposes of facilitating faster and higher-throughput imaging, a wide-field microscope was developed.[25] This custom-built wide-field RAMM microscope (ASI) was equipped with excitation light-emitting diodes (LEDs) (405, 505, and 590 nm) and an excitation polarizing filter (Edmund Optics, Barrington, NJ), and built to perform simultaneous two-color fluorescence anisotropy imaging. Images were collected using a 60×/1.42 NA oil immersion or a 40×/0.75 NA air objective lens (Olympus, Richmond Hill, Canada). Fluorescence was passed through a Cerulean (ET470/24M) or Venus (ET535/30M) emission filter on a filter wheel, and subsequently split using an Optosplit II (Cairn, Faversham, U.K.) to simultaneously collect parallel and perpendicular emission light on separate regions of an IRIS 15 CMOS camera (Teledyne Photometrics, Tucson, AZ).

Image Analysis. Parallel ($I_∥$) and perpendicular ($I_⊥$) fluorescence intensity images were analyzed with a custom ImageJ plugin. These are available at https://github.com/RocheleauLab/Optosplit-Anisotropy-Analysis-scripts. The images were background-corrected using a rolling ball filter. Pixel-by-pixel anisotropy (r) was calculated using the background-corrected intensities: $r = (I_∥ − GI_⊥)/(I_∥ + 2G_⊥)$.[26] The G factor for the two-photon microscope was measured by exciting samples with both vertically (V) polarized and horizontally (H) polarized light and collecting the polarized emission.[27,28] The G-factor for the wide-field microscope was calculated using fluorescein solutions, simplifying the standard anisotropy equation to $G = I_∥/I_⊥$. For images collected using the 1.42 NA objective lens, we used additional correction factors (K_a, K_b, and K_c) to account for the blurring of parallel and perpendicular intensities.[26] Cells were manually thresholded to remove cells of dim or saturated intensity, both of which can skew anisotropy results. Regions of interest (ROI) were selected using the parallel intensity images to avoid selection bias.

Statistics. All data are presented as mean ± standard error of the mean (S.E.M.) based on at least three separate experiment days (i.e., n = 3 independent trials). Each independent trial consists of at least five to more than 30 cells (5−30 technical replicates). Iglewicz and Hoaglin's robust test for multiple outliers was used to detect outliers from technical replicates. Statistical significance was determined using Prism 6 (GraphPad, San Diego, CA). Post hoc tests were used to determine significance between groups following one- or two-way analysis of variance (ANOVA). Tukey's multiple comparison tests were used when comparing between all groups. Dunnett's multiple comparison tests were used when comparing the control group vs other groups only. Sidak's multiple comparison tests were used for repeated-measures ANOVA. Anisotropy measurements were confirmed as normally distributed using a normal probability plot and D'Agostino−Pearson normality tests.

■ RESULTS

Determining the pH Sensitivity of Apollo-NADP$^+$. Fluorescent proteins are variably sensitive to pH, which could result in potential artifacts in the application of genetically encoded sensors. To select a fluorescent protein for Apollo-NADP$^+$ targeting, we first measured the impact of pH on the steady-state fluorescence anisotropy of fluorescent protein tandem dimers (EGFP, mVenus, mCerulean1, mCerulean3, and mTurquoise2) (Figure 1a,b). These tandem dimers are
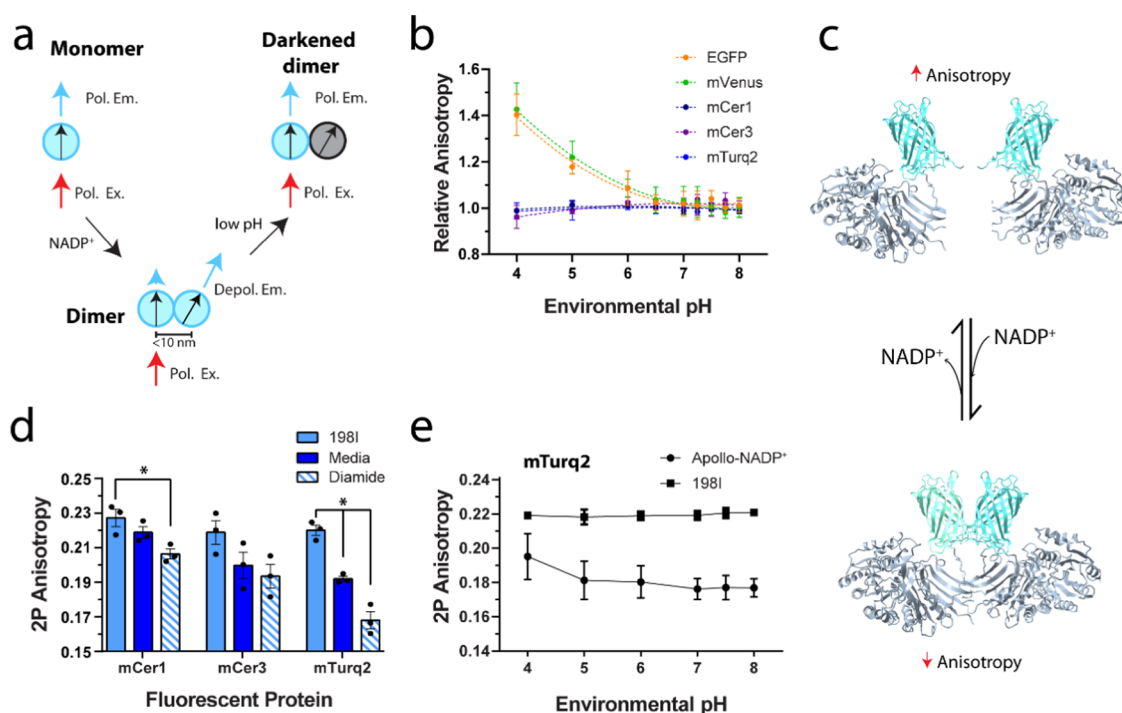
Figure 1. pH optimization of Apollo-NADP$^+$. (a) Polarized excitation of fluorescent proteins results in polarized emission and high steady-state fluorescence anisotropy (Monomer). HomoFRET occurs when the proteins are within 10 nm causing depolarization of the emission and a drop in steady-state anisotropy (Dimer). A drop in pH below the pK_a results in "darkening" (darkened dimer) and an artifactual increase in anisotropy. (b) Tandem dimers of EGFP, mVenus, mCerulean (mCer1), mCerulean3 (mCer3), and mTurquoise2 (mTurq2) were expressed in AD293 cells and imaged under varying pH. (c) Cartoon representation of the Apollo-NADP$^+$ sensor responding to NADP$^+$ through allosteric dimerization. The sensor is composed of enzymatically inactivated human G6PD tagged with fluorescent protein. The crystal structures of human G6PD (PDB 6E07) and yellow fluorescent proteins (PDB 3V3D) as a surrogate for the GFP-derived fluorescent proteins were used to generate the cartoon. Structures shown are not to scale or an exact representation of the amino acid sequence. (d) Apollo-NADP$^+$ and monomeric R198P-G6PD (R198I) tagged with mCer1, mCer3, and mTurq2 were imaged in AD293 cells in media. Apollo-NADP$^+$ was subsequently imaged after treatment with diamide (5 min, 5 mM), $n = 3$. (e) Cells expressing the mTurq2 versions of Apollo-NADP$^+$ and R198I were exposed to 5 mM diamide and imaged under varying pH, $n = 3$; * denotes significance <0.05.

connected by a short linker to ensure homoFRET,[29,30] thus mimicking the low anisotropy of dimeric Apollo-NADP$^+$ (Figure 1a). These data show consistently low anisotropy in the blue tandem dimers (mCer1, mCer3, mTurq2) across the full range of pH (Figure 1b). In contrast, the EGFP and mVenus tandem dimers showed a progressive increase in anisotropy below pH 6.0. This is consistent with the lower pK_a values of the bluer fluorescent proteins (3.7–4.7) compared to EGFP and mVenus (6.0 and 5.5, respectively). Dropping pH below the pK_a results in a fractional decrease in molecular brightness (darkening) of the fluorophore and an artifactual rise in anisotropy.

To further select from the blue fluorescent proteins, we compared the responses of mCer1-, mCer3-, and mTurq2-tagged Apollo-NADP$^+$ in response to NADPH oxidation by diamide (Figure 1c,d). NADP$^+$-induced dimerization of Apollo-NADP$^+$ decreases the steady-state fluorescence anisotropy due to homoFRET (Figure 1c). The blue sensors all showed a drop in anisotropy in response to diamide treatment compared to monomeric control (R198I) and sensor in normal media, with the largest responses found in cells expressing mTurq2-Apollo-NADP$^+$ (Figure 1d). These responses tracked well with the quantum yield (QY) of each fluorescent protein (mTurq2 (0.93) > mCer3 (0.87) ≫ mCer1 (0.49)).[31] This trend is consistent with the single fluorescent protein acting as both donor, impacting Förster distance ($R_0 \propto (\text{QY}_D)^{1/2}$), and acceptor, impacting the energy transmitted as depolarized

fluorescence ($I_A \propto \text{QY}_A$). We subsequently settled upon the mTurq2 version as the most dynamic sensor.

We were concerned pH could also impact dimerization of the catalytically inactive G6PD. To determine the impact of pH on sensor dimerization, we next compared the fluorescence anisotropy of Apollo-NADP$^+$ (mTurq2-Apollo-NADP$^+$) and R198I in cells treated with diamide (Figure 1e). These data show stable sensor dimerization across a wide range of pH, with increased anisotropy found below pH 5.0. This suggests G6PD, which translocates between the cytoplasm and peroxisome, evolved to withstand variations in pH.[32−34] Overall, mTurq2-Apollo-NADP$^+$ was the most dynamic of the pH-stable sensors, and thus was chosen for subsequent organelle targeting.

Organelle Targeting of mTurq2-Apollo-NADP$^+$. We added targeting sequences for the mitochondrial matrix, nucleus, ER lumen, plasma membrane, and peroxisome to mTurq2-Apollo-NADP$^+$. To confirm organelle-specific localization, we imaged each sensor in INS-1E (Figure 2a) and AD293 cells (Figure S1) using a wide-field and two-photon microscope, respectively. These data show the expected morphology for each organelle.[35] To validate the activity of the sensors, we imaged a corresponding set of targeted controls (blue) and the sensors expressed in INS-1E beta-cells (Figure 2b). The cells were then treated with glucose (0, 1, and 15 mM; red) and hydrogen peroxide (0.1, 10, and 1000 μM H$_2$O$_2$; yellow) to, respectively, reduce and oxidize cellular
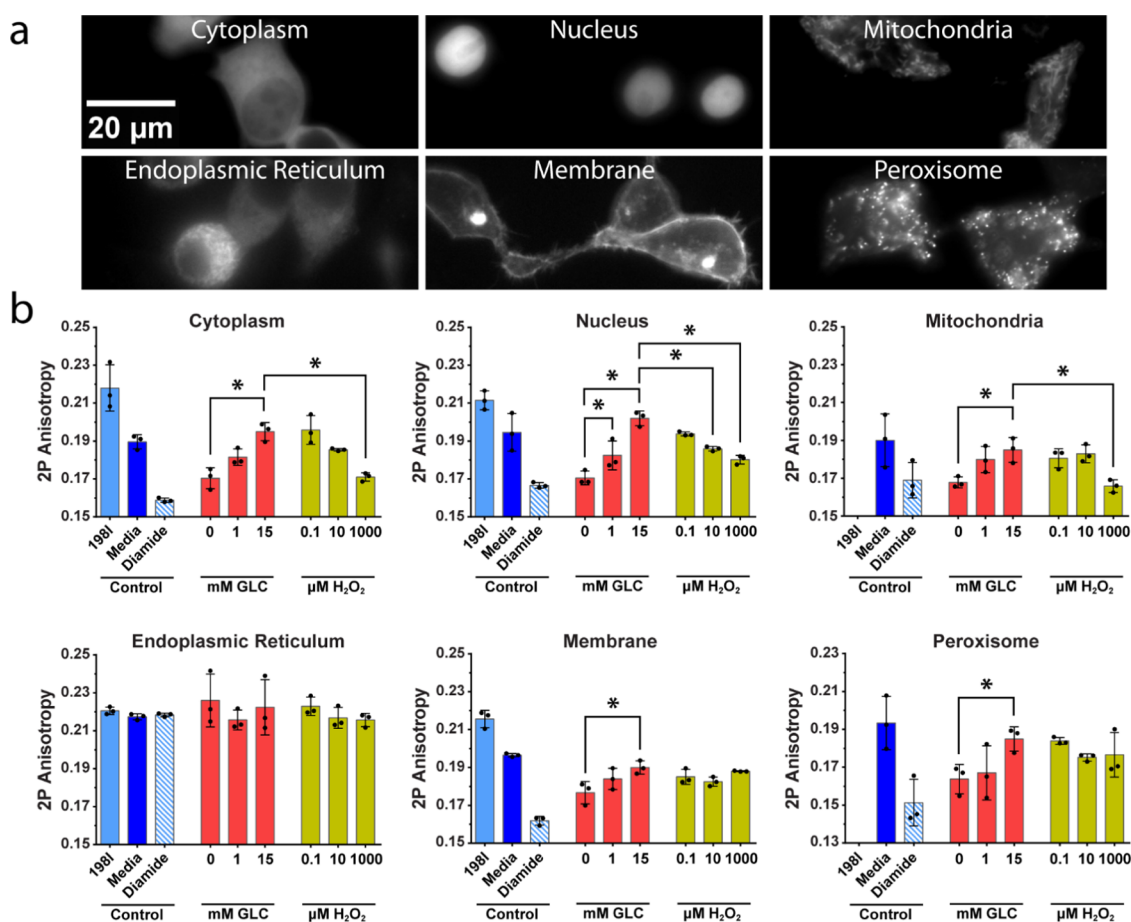
Figure 2. Characterization of organelle-targeted Apollo-NADP$^+$ constructs. (a) Representative wide-field intensity images of mTurq2-Apollo-NADP$^+$ expressed in INS-1E cells to demonstrate the sensor shows correct organelle morphology and localizes to various subcellular compartments. (b) mTurq2-Apollo-NADP$^+$ and R198I constructs targeted to each organelle were expressed in INS-1E beta-cells. Controls included the R198I monomeric control (198I, where expressed), Apollo-NADP$^+$ in full media (media), and 5 mM diamide (diamide). The sensor was imaged using a two-photon microscope in sequential response to glucose and H$_2$O$_2$, n = 3. Not shown are the R198I values for the mitochondria (0.178 ± 0.002) and the peroxisome (0.097 ± 0.002) as the low intensity of the images and the variance in anisotropy suggested that these constructs did not properly refold when targeted to these organelles; * denotes significance <0.05.

NADPH/NADP$^+$ redox state (Figure 2b). Targeted controls included R198I monomers and cells expressing the corresponding sensor in response to culture media and to diamide. These controls defined the photophysical range of each sensor (i.e., monomer-to-dimer), except in the mitochondria and peroxisome where R198I did not consistently localize to the organelle. The inability of R198I to express in these organelles suggests that the already destabilized construct is unable to fold in these organelles.[36] Notably, the anisotropy values of the targeted R198I constructs across all of the other organelles only showed a ±0.007 or 3.3% standard deviation demonstrating the precision of anisotropy imaging. Thus, any of the R198I versions could potentially serve as a monomeric control for the mitochondria and peroxisome.

Sensor targeted to the cytoplasm, mitochondria, and nucleus all showed rises in anisotropy induced by glucose and falls in anisotropy induced by H$_2$O$_2$ directionally consistent with reduction and oxidation of the NADPH/NADP$^+$ redox state (Figure 2b, top). While the nuclear and cytoplasmic responses mirrored each other, the mitochondrial response to H$_2$O$_2$ was dampened, only showing a significant response at 1000 μM H$_2$O$_2$. This could be due to cytoplasmic H$_2$O$_2$-scavenging prior to reaching the organelle and by greater antioxidant capacity at high glucose. In contrast, ER-targeted sensor

showed an elevated anisotropy with no response to any of these treatments (Figure 2b, bottom left). INS-1E and AD293 cells targeted with ER sensor also showed no response to cortisone/hydrocortisone (data not shown), a treatment that affects ER NADPH/NADP$^+$ redox state via 11β-HSD-1,[37] effectively confirming that the ER sensor was nonfunctional. Membrane-targeted sensor showed a statistically significant response to glucose; however, the sensor did not subsequently respond to H$_2$O$_2$, suggesting an irreversible/slow recovery of monomerization due to molecular crowding in 2D at the membrane surface (Figure 2b, bottom middle). Finally, the peroxisomal sensor showed a significant response to high glucose, but a much smaller response to H$_2$O$_2$. The glucose response is consistent with peroxisomes generating NADPH using G6PD and/or IDH1.[32−34,38] The smaller H$_2$O$_2$ response could be attributed to catalase activity in peroxisomes detoxifying H$_2$O$_2$ without consuming NADPH. Overall, these data show functional Apollo-NADP$^+$ sensors in the cytoplasm, nucleus, mitochondrial matrix, and peroxisome.

Imaging Organelle-Specific Apollo-NADP$^+$ to Explore Glucose- and Glutamine-Stimulated NADPH Responses. Due to limited G6PD activity in beta-cells, glucose-stimulated NADPH production primarily depends on mitochondrial efflux of citrate/isocitrate and IDH1 activity.[3] To measure this
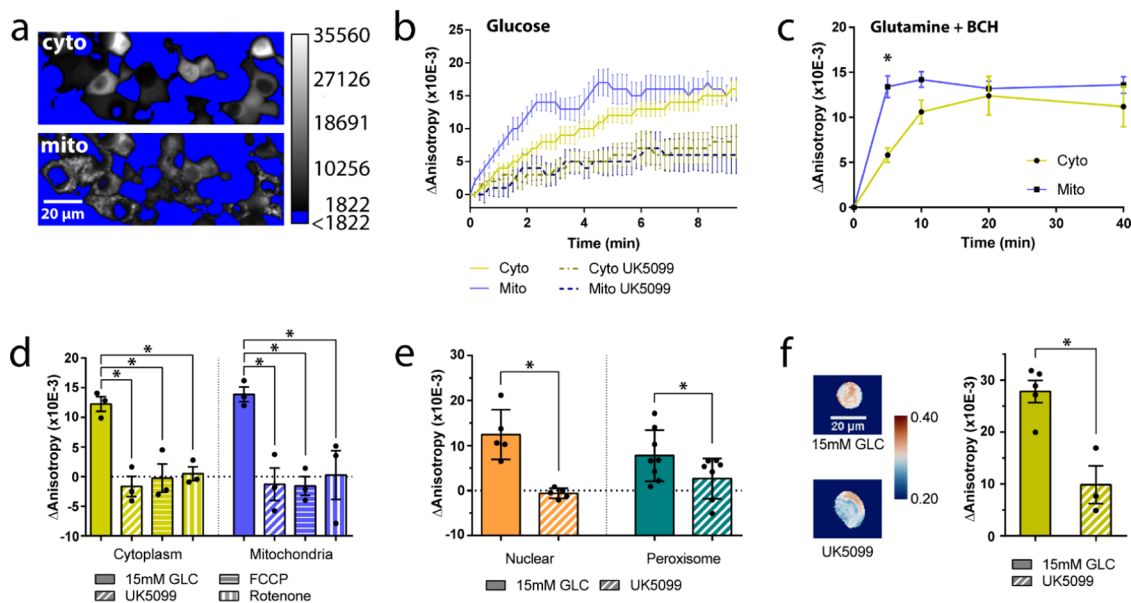
Figure 3. Using organelle-specific Apollo-NADP⁺ to determine the role of mitochondrial metabolism on NADPH responses. (a) Representative wide-field images of INS1E cells coexpressing mVenus-Apollo-NADP⁺ (Cyto) and mTurq2-Apollo-NADP⁺ (Mito) with similar thresholding and a 1 pixel median filter. Images have a HiLo lookup table applied, where blue represents background intensity, grayscale represents increasing intensity, and red represents saturated pixels. (b) Temporal response to 15 mM glucose bolus was compared to cells pretreated for 1 h with 50 μM UK5099. Data are reported as mean change in anisotropy (Δanisotropy ($\times 10^{-3}$)) $\pm$ S.E.M., $n = 5$. (c) Temporal response to 10 mM BCH in cells pretreated with glutamine (5 mM, 1 h), $n = 5$. (d) Anisotropy response to glucose (1−15 mM, 5 min) in control cells and cells pretreated with UK5099 (50 μM, 1 h), FCCP (1 μM, 5 min), and rotenone (1 μM, 5 min), $n = 3$. (e) Anisotropy responses to a 10 (nuclear) or 20 (peroxisome) min glucose bolus in cells pretreated with UK5099, $n = 5−8$. ((f), left) Representative anisotropy images of dispersed mouse islet cells transduced with cytoplasmic Apollo-NADP⁺ with similar thresholding and a 1 pixel median filter. Both cells were treated with 15 mM glucose (5 min), while the bottom cell was also pretreated with UK5099 (50 μM, 1 h). The color map is Vik.[39] ((f), right) Anisotropy responses to 15 mM glucose in controls or cells pretreated with UK5099, $n = 3−5$. Control replicates are shared with Figure 4f since the data were collected at the same time; * denotes significance <0.05.

metabolic route, we coexpressed cytoplasmic mVenus-Apollo-NADP⁺ and mitochondrial mTurq2-Apollo-NADP⁺ in INS-1E cells and simultaneously imaged the glucose-stimulated temporal responses (Figure 3a,b). These data show NADPH generation plateaus in the mitochondrial matrix at ~5 min (blue) while the cytoplasmic response was still rising at 9 min (yellow). We interpret this difference to indicate that mitochondrial metabolism drives the cytoplasmic response, but with the caveat that the difference in saturation time would be amplified by the smaller volume of the mitochondrial matrix. Further comparison of the individual cell anisotropy values against their associated parallel intensity values (Figure S2) showed that the anisotropy is independent of sensor concentration; thus, this earlier mitochondrial response is not a concentration-dependent artifact. Both responses were also significantly diminished by the mitochondrial pyruvate transport inhibitor UK5099. Together, these data are consistent with cytoplasmic NADPH production involving mitochondrial metabolism of pyruvate.

Glutamine is converted to the mitochondrial metabolite α-ketoglutarate through glutamate dehydrogenase (GDH) when triggered by the nonmetabolizable leucine analogue BCH.[40] GDH activity also generates mitochondrial NADH to drive mitochondrial membrane potential.[41] To confirm mitochondrial metabolism leads to cytoplasmic NADPH generation, we measured the cytoplasmic and mitochondrial response to glutamine and BCH (Figure 3c). These data show glutamine stimulates mitochondrial NADPH prior to the cytoplasm and supports a model where the cytoplasmic response depends on mitochondrial metabolism. Zhang et al. noted that glutamine/

BCH stimulation increased beta-cell reductive TCA flux, which would consume and thus depend on mitochondrial NADPH. In the absence of an initial drop in mitochondrial NADPH, we postulate that NADH derived from GDH activity supports NADPH production via NNT and consequent reductive TCA flux.

To further explore the link between mitochondrial and cytoplasmic NADPH generation, we simultaneously imaged the cytoplasmic and mitochondrial responses in cells treated with UK5099 and various electron transport chain inhibitors (Figures 3d and S3). UK5099 abolished the glucose-stimulated cytoplasmic and mitochondrial responses. The glucose-stimulated responses were also blocked by collapse of the mitochondrial membrane potential (FCCP) and inhibition of the electron transport chain (rotenone). However, the cytoplasmic mVenus sensor showed a small elevation in response to FCCP and rotenone that could potentially be due to a reduction in cytoplasmic pH[42] (Figure S3a). To confirm the glucose-stimulated responses, we repeated the same treatments in INS-1E cells expressing pH-insensitive cytoplasmic mTurq2 sensor (Figure S3b). These data show no response to FCCP and rotenone treatment and subsequent blocking of the glucose-stimulated response. Collectively, these data suggest that both mitochondrial membrane potential and mitochondrial NADPH accumulation are required for a subsequent NADPH response in the cytoplasm.

To measure the impact of pyruvate entry into mitochondrial metabolism on other organelles, we imaged glucose-stimulated responses in the nucleus and peroxisome in the presence of UK5099 (Figures 3e and S4). These data show blocking
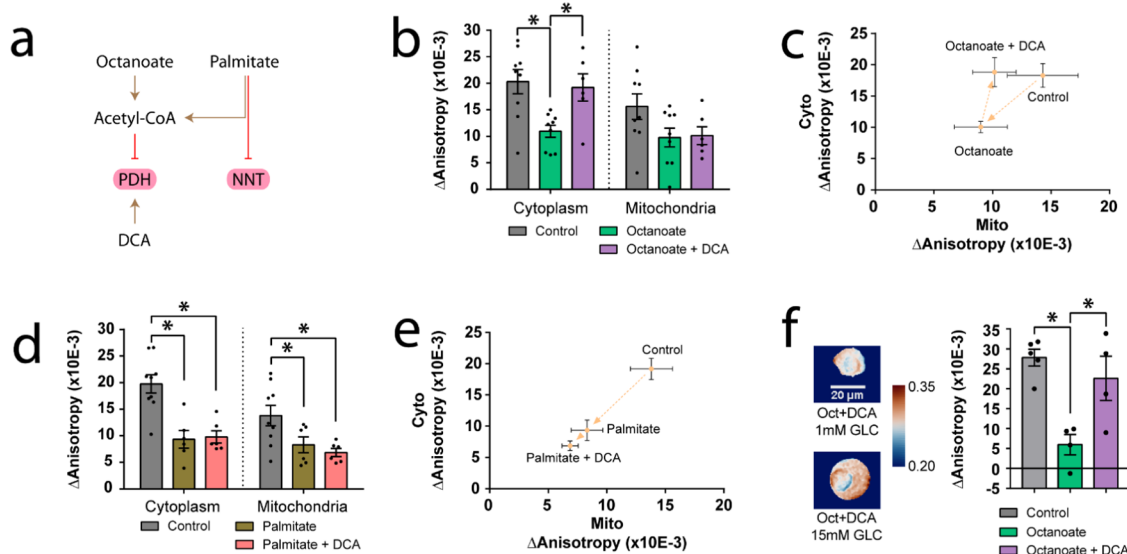
Figure 4. Using organelle-specific Apollo-NADP$^+$ to determine the roles of nonanaplerotic fatty acids and NNT activity on cytoplasmic and mitochondrial NADPH. (a) Acetyl-CoA produced by beta-oxidation of both fatty acids will inhibit pyruvate dehydrogenase (PDH) activity with dichloroacetate (DCA) reversing this effect. Longer-chain fatty acid palmitate is also a direct inhibitor of NNT. (b) Simultaneous wide-field imaging of cytoplasmic and mitochondrial anisotropy responses to 15 mM glucose (15 min) in cells pretreated with octanoate (400 μM, 30 min), octanoate +1 μM DCA (30 min), or no treatment (control). Data are reported as the mean change in anisotropy (Δanisotropy ($\times 10^{-3}$)) $\pm$ S.E.M., $n = 6-9$. (c) Same anisotropy changes from (b) shown in scatter plot. Dotted arrows denote the order they are described in the results. (d, e) Simultaneous wide-field imaging of cytoplasmic and mitochondrial anisotropy responses to 15 mM glucose (15 min) in cells pretreated with palmitate only (400 μM, 4 h), or palmitate (4 h) + 1 μM DCA (30 min) after a 15 mM glucose bolus, $n = 5-9$. ((f), left) Representative wide-field anisotropy images of dispersed mouse islets transduced with cytoplasmic Apollo-NADP$^+$ with similar thresholding and a 1 pixel median filter. Cells were stimulated with 15 mM glucose (15 min) after pretreatment in 400 μM octanoate (30 min, top) or 400 μM octanoate + 1 μM DCA (30 min, bottom). ((f), right) Anisotropy responses of controls compared to cells pretreated with octanoate or octanoate + DCA, $n = 4-5$. Control replicates are shared with Figure 3f since the data were collected at the same time; * denotes significance <0.05.

pyruvate entry into mitochondrial metabolism abolishes responses in the nucleus and peroxisome. Overall, these data suggest mitochondrial NADPH accumulation precedes cytoplasmic, nuclear, and peroxisomal NADPH generation, which are thus all dependent on mitochondrial metabolism (e.g., citrate/isocitrate efflux).

To validate our findings in primary tissue, we imaged the glucose-stimulated response of dispersed mouse islet cells transduced with cytoplasmic mVenus-Apollo-NADP$^+$ (Figure 3f). The glucose-stimulated response was abolished by UK5099 consistent with cytoplasmic NADPH generation being due to mitochondrial pyruvate metabolism in primary beta-cells.

Imaging Organelle-Specific Apollo-NADP$^+$ to Probe the Impact of Fatty Acids on Glucose-Stimulated NADPH Response. Fatty acids impact glucose-stimulated NADPH production through inhibition of pyruvate dehydrogenase (PDH) activity by acetyl-CoA[43] and through inhibition of mitochondrial NNT activity at higher chain lengths[44] (Figure 4a). To measure the impact of PDH inactivation on glucose-stimulated NADPH responses, we coexpressed cytoplasmic (mVenus) and mitochondrial (mTurq2) sensors to simultaneously image the glucose-stimulated responses of octanoate-treated cells (Figure 4b,c). The cytoplasmic and mitochondrial sensors showed no response to octanoate and the PDH activator DCA suggesting NADPH generation in both organelles depends on anaplerotic metabolism (Figure S5a,b). Octanoate treatment decreased the subsequent glucose-stimulated cytoplasmic response with minimal impact on the mitochondrial response (Figure 4b,c). Consistent with octanoate inactivation of PDH, DCA restored the cytoplasmic

response while leaving the mitochondrial response unaffected. The inability of octanoate to block mitochondrial NADPH generation suggested a prominent role for NNT. NNT converts NADH to NADPH using mitochondrial membrane potential, thus linking mitochondrial energetics to antioxidant capacity.[8] To confirm the role of NNT in the glucose-stimulated mitochondrial NADPH response, we next pretreated cells with palmitate, a longer-chain fatty acid well established to inhibit NNT activity (Figures 4d,e and S5c,d).[44] Palmitate requires transport by carnitine palmitoyltransferases, resulting in a longer preincubation time. Palmitate also showed no impact on the baseline sensor responses (Figure S5c,d) but abolished both the cytoplasmic and mitochondrial glucose-stimulated responses in line with inhibition of PDH and NNT (via palmitoyl-CoA) (Figure 4d,e). In contrast to octanoate, the cytoplasmic response in the presence of palmitate was unaffected by DCA. We therefore postulate that the cytoplasmic NADPH response depends on both oxidative (PDH) and anaplerotic (PC) entry of pyruvate into the TCA cycle and mitochondrial NADPH generation by NNT.

To validate these findings in primary tissue, we imaged the impact of octanoate on the glucose-stimulated response of dispersed mouse islet cells transduced with cytoplasmic mVenus-Apollo-NADP$^+$ (Figures 4f and S6). Octanoate significantly diminished the glucose-stimulated NADPH response, and this response was restored by activation of PDH using DCA. These data suggest the cytoplasmic NADPH response is dependent on mitochondrial efflux in primary cells.

DISCUSSION AND CONCLUSIONS

Our goal was to target Apollo-NADP⁺ to organelles to measure NADPH generation and compartmentalization in beta-cells. In contrast to the cytoplasm,[45] ER,[46] and nucleus,[47] the mitochondrial matrix[48] and peroxisome[49] can show significant variability in physiological pH. This variability complicates the application of genetically encoded sensors in these organelles. Although some pH sensitivity is not insurmountable, the methods to correct for it (e.g., coexpressing a pH sensor or an inactivated sensor)[14,45] work against the ability to track single cells and perform multiparametric imaging. Since Apollo-NADP⁺ sensors are single-color sensors, we were able to overcome this limitation by swapping in different fluorescent proteins. In general, the bluer fluorescent protein dimers (mCer1, mCer3, and mTurq2) were more pH-stable than the greener fluorescent protein dimers (mVen, EGFP) likely due to lower pK_a ($pK_a \sim 3.2$).[31,50] We subsequently settled upon the mTurq2 version as the most dynamic sensor noting the sensor responses tracked well with the QY of each fluorescent protein (mTurq2 (0.93) > mCer3 (0.87) ≫ mCer1 (0.49)).[31] This trend is consistent with the single fluorescent protein acting as both donor to impact Förster distance ($R_0 \propto (QY_D)^{1/2}$) and acceptor to impact the energy transmitted as depolarized fluorescence ($I_A \propto QY_A$). Thus, we targeted the mTurq2 version of the sensor due to having the highest pH stability and apparent dynamic range.

Highlighting the versatility of Apollo sensors, we proceeded with single (mTurq2)- and dual-color (mTurq2 and mVenus) imaging of organelle-targeted Apollo-NADP⁺ sensors to examine beta-cell NADPH production. We showed glucose- and glutamine-stimulated NADPH production in the mitochondria plateaued prior to the cytoplasm, with both the glucose-stimulated responses blocked by the pyruvate transport inhibitor UK5099. These responses were also independent of the concentration of the sensor. We interpreted the difference in response times to indicate that cytoplasmic NADPH generation depends on earlier mitochondrial metabolism. One caveat to this interpretation is that the temporal differences may reflect the relative volumes of the cytoplasm and mitochondrial matrix. Although we cannot refute the role of pool volumes based on our data, previous work in rat liver suggests mitochondria hold more than half the total cellular NADP(H) despite having a much smaller volume.[51] The interconversion of NADP⁺ to NADPH is thus unlikely to be shorter in mitochondria due to pool size. It is also important to consider free NADP(H) levels since the majority is in the bound state and the sensors respond to free NADP⁺. Previous work measured free NADPH concentrations in the cytoplasm and mitochondrial matrix to be 3.1 and 37 μM, respectively.[13] NADPH/NADP⁺ ratios have been reported in the range of 15−333 for the cytoplasm[13,52,53] and 175.3−218.7 for the mitochondrial matrix.[16] Based on these estimated ratios and free NADPH concentrations, the expected free NADP⁺ concentrations are 0.0093−0.21 μM for cytoplasm and 0.17−0.21 μM for mitochondrial matrix. This suggests mitochondrial concentrations of free NADP⁺ are 1- to 23-fold higher than the cytoplasm. Our temporal data shows faster NADPH saturation in the mitochondria. Since the mitochondrial matrix is expected to have similar or greater concentrations of total NADP(H) and free NADP⁺, we believe our results cannot be explained solely by differences in organelle volume and/or free NADP⁺ concentrations.

Our data demonstrate how low G6PD activity in beta-cells leaves glucose-stimulated NADPH production in the cytoplasm dependent on mitochondrial efflux. Pyruvate enters beta-cell mitochondrial refilling of TCA cycle intermediates (i.e., anaplerosis), triggering mitochondrial citrate/isocitrate efflux and subsequent production of cytoplasmic NADPH via ME and/or IDH1. To examine the source of glucose-stimulated mitochondrial NADPH generation, we measured the impact of short (octanoate) and longer-chain (palmitate) fatty acids on the glucose-stimulated mitochondrial and cytoplasmic responses. We postulated that inhibition of PDH by acetyl-CoA would lessen cytoplasmic NADPH response by decreasing metabolic flux through citrate synthase and/or increasing isocitrate consumption by NAD⁺-dependent isocitrate dehydrogenase (IDH3). Consistently, blocking PDH through the short-chain fatty acid octanoate inhibited cytoplasmic, but not mitochondrial, NADPH generation. Additionally, DCA treatment led to PDH activation and rescued the cytoplasmic response. Finally, previous work suggests that mitochondrial membrane potential-driven NNT activity greatly contributes to glucose-stimulated mitochondrial NADPH production.[6,8,54] Consistently, the glucose-stimulated cytoplasmic and mitochondrial NADPH responses were abolished by inhibiting NNT using palmitate and by blocking mitochondrial membrane potential.

The glucose-stimulated nuclear and peroxisomal responses were also blocked by UK5099. Notably, the nuclear response mirrored the cytoplasmic response consistent with previous work suggesting NADPH is readily diffusible between cytoplasmic and nuclear compartments.[14] Thus, the nuclear targeted sensor could potentially serve as a useful surrogate for the cytoplasmic sensor to improve spatial separation during multiparameter imaging and to better isolate individual cell responses in tissues. However, substitution of the nuclear sensor will need to be fully considered in the context of varied compartmentalization of glutathione in the nucleus during the cell cycle.[13,55,56] Overall, this work expands the Apollo-NADP⁺ family of sensors while suggesting a dominant role of mitochondrial metabolism in setting beta-cell NADPH/NADP⁺ redox state across organelles.

ASSOCIATED CONTENT

Ⓢ Supporting Information

The Supporting Information is available free of charge at https://pubs.acs.org/doi/10.1021/acssensors.2c01174.

> Organelle-targeted Turq2-Apollo-NADP⁺ sensor expression in AD293 cells (Figure S1); relationship between individual cell anisotropy and parallel intensity in the cytoplasmic and mitochondrial sensor (Figure S2); impact of drug treatments on NADPH baseline in cytoplasmic and mitochondrial sensors (Figure S3); impact of UK5099 on NADPH baseline in nuclear and peroxisomal Turq2 sensors (Figure S4); impact of fatty acid and DCA treatment on baseline NADPH levels in cytoplasmic and mitochondrial sensors (Figure S5); and impact of UK5099, octanoate, and DCA to pre-glucose NADPH levels in mouse dispersed islets (Figure S6) (PDF)

■ AUTHOR INFORMATION

Corresponding Author

Jonathan V. Rocheleau — *Institute of Biomedical Engineering, University of Toronto, Toronto, Ontario M5S 3G9, Canada; Toronto General Hospital Research Institute, University Health Network, Toronto, Ontario M5G 2C4, Canada; Department of Physiology, University of Toronto, Toronto, Ontario M5S 1A8, Canada; Banting and Best Diabetes Centre, University of Toronto, Toronto, Ontario M5G 2C4, Canada;* ⓞ orcid.org/0000-0002-1760-2564; Email: jon.rocheleau@utoronto.ca

Authors

Huntley H. Chang — *Institute of Biomedical Engineering, University of Toronto, Toronto, Ontario M5S 3G9, Canada; Toronto General Hospital Research Institute, University Health Network, Toronto, Ontario M5G 2C4, Canada;* ⓞ orcid.org/0000-0003-3181-8019

Alex M. Bennett — *Institute of Biomedical Engineering, University of Toronto, Toronto, Ontario M5S 3G9, Canada; Toronto General Hospital Research Institute, University Health Network, Toronto, Ontario M5G 2C4, Canada*

William D. Cameron — *Institute of Biomedical Engineering, University of Toronto, Toronto, Ontario M5S 3G9, Canada; Toronto General Hospital Research Institute, University Health Network, Toronto, Ontario M5G 2C4, Canada*

Eric Floro — *Institute of Biomedical Engineering, University of Toronto, Toronto, Ontario M5S 3G9, Canada; Toronto General Hospital Research Institute, University Health Network, Toronto, Ontario M5G 2C4, Canada*

Aaron Au — *Institute of Biomedical Engineering, University of Toronto, Toronto, Ontario M5S 3G9, Canada*

Christopher M. McFaul — *Institute of Biomedical Engineering, University of Toronto, Toronto, Ontario M5S 3G9, Canada*

Christopher M. Yip — *Institute of Biomedical Engineering, University of Toronto, Toronto, Ontario M5S 3G9, Canada;* ⓞ orcid.org/0000-0003-4507-556X

Complete contact information is available at:
https://pubs.acs.org/10.1021/acssensors.2c01174

Author Contributions

[⊥]H.H.C. and A.M.B. contributed equally to this work. H.H.C., A.M.B., W.D.C., and J.V.R. designed research. H.H.C., A.M.B., W.D.C., and E.F. performed research. H.H.C., A.M.B., W.D.C., and E.F. analyzed data. A.A., C.M.M., and C.M.Y. provided technical expertise. H.H.C. and J.V.R. wrote the paper.

Notes

The authors declare no competing financial interest.
The authors declare no competing interests. This manuscript has been deposited in bioRxiv.[57]

■ ACKNOWLEDGMENTS

■ REFERENCES

(1) Ying, W. NAD+/NADH and NADP+/NADPH in Cellular Functions and Cell Death: Regulation and Biological Consequences. *Antioxid. Redox Signaling* **2008**, *10*, 179−206.

(2) Tran, D. H.; Kesavan, R.; Rion, H.; Soflaee, M. H.; Solmonson, A.; Bezwada, D.; Vu, H. S.; Cai, F.; Phillips, J. A.; DeBerardinis, R. J.; Hoxhaj, G. Mitochondrial NADP+ Is Essential for Proline Biosynthesis during Cell Growth. *Nat. Metab.* **2021**, *3*, 571−585.

(3) Schuit, F.; De Vos, A.; Farfari, S.; Moens, K.; Pipeleers, D.; Brun, T.; Prentki, M. Metabolic Fate of Glucose in Purified Islet Cells: Glucose-regulated Anaplerosis in Beta Cells. *J. Biol. Chem.* **1997**, *272*, 18572−18579.

(4) MacDonald, M. J. Feasibility of a Mitochondrial Pyruvate Malate Shuttle in Pancreatic Islets. Further Implication of Cytosolic NADPH in Insulin Secretion. *J. Biol. Chem.* **1995**, *270*, 20051−20058.

(5) Pongratz, R. L.; Kibbey, R. G.; Shulman, G. I.; Cline, G. W. Cytosolic and Mitochondrial Malic Enzyme Isoforms Differentially Control Insulin Secretion. *J. Biol. Chem.* **2007**, *282*, 200−207.

(6) Rydström, J. Mitochondrial NADPH, Transhydrogenase and Disease. *Biochim. Biophys. Acta, Bioenerg.* **2006**, *1757*, 721−726.

(7) Ronnebaum, S. M.; Ilkayeva, O.; Burgess, S. C.; Joseph, J. W.; Lu, D.; Stevens, R. D.; Becker, T. C.; Sherry, A. D.; Newgard, C. B.; Jensen, M. V. A Pyruvate Cycling Pathway Involving Cytosolic NADP-Dependent Isocitrate Dehydrogenase Regulates Glucose-Stimulated Insulin Secretion. *J. Biol. Chem.* **2006**, *281*, 30593−30602.

(8) Vogel, R.; Wiesinger, H.; Hamprecht, B.; Dringen, R. The Regeneration of Reduced Glutathione in Rat Forebrain Mitochondria Identifies Metabolic Pathways Providing the NADPH Required. *Neurosci. Lett.* **1999**, *275*, 97−100.

(9) Toye, A. A.; Lippiat, J. D.; Proks, P.; Shimomura, K.; Bentley, L.; Hugill, A.; Mijat, V.; Goldsworthy, M.; Moir, L.; Haynes, A.; Quarterman, J.; Freeman, H. C.; Ashcroft, F. M.; Cox, R. D. A Genetic and Physiological Study of Impaired Glucose Homeostasis Control in C57BL/6J Mice. *Diabetologia* **2005**, *48*, 675−686.

(10) Aston-Mourney, K.; Wong, N.; Kebede, M.; Zraika, S.; Balmer, L.; McMahon, J. M.; Fam, B. C.; Favaloro, J.; Proietto, J.; Morahan, G.; Andrikopoulos, S. Increased Nicotinamide Nucleotide Transhydrogenase Levels Predispose to Insulin Hypersecretion in a Mouse Strain Susceptible to Diabetes. *Diabetologia* **2007**, *50*, 2476−2485.

(11) Fergusson, G.; Éthier, M.; Guévremont, M.; Chrétien, C.; Attané, C.; Joly, E.; Fioramonti, X.; Prentki, M.; Poitout, V.; Alquier, T. Defective Insulin Secretory Response to Intravenous Glucose in C57Bl/6J Compared to C57Bl/6N Mice. *Mol. Metab.* **2014**, *3*, 848−854.

(12) Freeman, H. C.; Hugill, A.; Dear, N. T.; Ashcroft, F. M.; Cox, R. D. Deletion of Nicotinamide Nucleotide Transhydrogenase. *Diabetes* **2006**, *55*, 2153−2156.

(13) Tao, R.; Zhao, Y.; Chu, H.; Wang, A.; Zhu, J.; Chen, X.; Zou, Y.; Shi, M.; Liu, R.; Su, N.; Du, J.; Zhou, H.-M.; Zhu, L.; Qian, X.; Liu, H.; Loscalzo, J.; Yang, Y. Genetically Encoded Fluorescent Sensors Reveal Dynamic Regulation of NADPH Metabolism. *Nat. Methods* **2017**, *14*, 720−728.

(14) Moon, S. J.; Dong, W.; Stephanopoulos, G. N.; Sikes, H. D. Oxidative Pentose Phosphate Pathway and Glucose Anaplerosis Support Maintenance of Mitochondrial NADPH Pool under Mitochondrial Oxidative Stress. *Bioeng. Transl. Med.* **2020**, *5*, No. e10184.

(15) Zhao, F.-L.; Zhang, C.; Zhang, C.; Tang, Y.; Ye, B.-C. A Genetically Encoded Biosensor for in Vitro and in Vivo Detection of NADP+. *Biosens. Bioelectron.* **2015**, *77*, 901−906.

(16) Sallin, O.; Reymond, L.; Gondrand, C.; Raith, F.; Koch, B.; Johnsson, K. Semisynthetic Biosensors for Mapping Cellular Concentrations of Nicotinamide Adenine Dinucleotides. *eLife* **2018**, *7*, No. e32638.

(17) Cameron, W. D.; Bui, C. V.; Hutchinson, A.; Loppnau, P.; Gräslund, S.; Rocheleau, J. V. Apollo-NADP+: A Spectrally Tunable Family of Genetically Encoded Sensors for NADP+. *Nat. Methods* **2016**, *13*, 352−358.

(18) Warren, S. C.; Margineanu, A.; Katan, M.; Dunsby, C.; French, P. M. W. Homo-FRET Based Biosensors and Their Application to Multiplexed Imaging of Signalling Events in Live Cells. *Int. J. Mol. Sci.* **2015**, *16*, 14695−14716.

(19) Ross, B. L.; Tenner, B.; Markwardt, M. L.; Zviman, A.; Shi, G.; Kerr, J. P.; Snell, N. E.; Mcfarland, J. J.; Mauban, J. R.; Ward, C. W.; Rizzo, M. A.; Zhang, J. Single-Color, Ratiometric Biosensors for Detecting Signaling Activities in Live Cells. *eLife* **2018**, *7*, No. e35458.

(20) Mahato, R. I.; Smith, L. C.; Rolland, A. Pharmaceutical Perspectives of Nonviral Gene Therapy. In *Advances in Genetics*; Hall, J. C.; Dunlap, J. C.; Friedmann, T.; Gianelli, F., Eds.; Acadenuc Press, 1999; Chapter 4, Vol. *41*, pp 95−156.

(21) Gould, S. J.; Keller, G.-A.; Hosken, N.; Wilkinson, J.; Subramani, S. A Conserved Tripeptide Sorts Proteins to Peroxisomes. *J. Cell Biol.* **1989**, *108*, 1657−1664.

(22) Loiselle, F. B.; Casey, J. R. Measurement of Intracellular PH. *Methods Mol. Biol.* **2010**, *637*, 311−331.

(23) Sun, M. Y.; Yoo, E.; Green, B. J.; Altamentova, S. M.; Kilkenny, D. M.; Rocheleau, J. V. Autofluorescence Imaging of Living Pancreatic Islets Reveals Fibroblast Growth Factor-21 (FGF21)-Induced Metabolism. *Biophys. J.* **2012**, *103*, 2379−2388.

(24) Pal, V.; Wang, Y.; Regeenes, R.; Kilkenny, D. M.; Rocheleau, J. V. Laminin Matrix Regulates Beta-Cell FGFR5 Expression to Enhance Glucose-Stimulated Metabolism. *Sci. Rep.* **2022**, *12*, No. 6110.

(25) Cameron, W. D.; Bennett, A. M.; Bui, C. V.; Chang, H. H.; Rocheleau, J. V. Leveraging Multimodal Microscopy to Optimize Deep Learning Models for Cell Segmentation. *APL Bioeng.* **2021**, *5*, No. 016101.

(26) Axelrod, D. Carbocyanine Dye Orientation in Red Cell Membrane Studied by Microscopic Fluorescence Polarization. *Biophys. J.* **1979**, *26*, 557−573.

(27) Blackman, S. M.; Cobb, C. E.; Beth, A. H.; Piston, D. W. The Orientation of Eosin-5-Maleimide on Human Erythrocyte Band 3 Measured by Fluorescence Polarization Microscopy. *Biophys. J.* **1996**, *71*, 194−208.

(28) Rocheleau, J. V.; Edidin, M.; Piston, D. W. Intrasequence GFP in Class I MHC Molecules, a Rigid Probe for Fluorescence Anisotropy Measurements of the Membrane Environment. *Biophys. J.* **2003**, *84*, 4078−4086.

(29) Ming, A. Y. K.; Yoo, E.; Vorontsov, E. N.; Altamentova, S. M.; Kilkenny, D. M.; Rocheleau, J. V. Dynamics and Distribution of Klotho*β* (KLB) and Fibroblast Growth Factor Receptor-1 (FGFR1) in Living Cells Reveal the Fibroblast Growth Factor-21 (FGF21)-Induced Receptor Complex. *J. Biol. Chem.* **2012**, *287*, 19997−20006.

(30) Regeenes, R.; Silva, P. N.; Chang, H. H.; Arany, E. J.; Shukalyuk, A. I.; Audet, J.; Kilkenny, D. M.; Rocheleau, J. V. Fibroblast Growth Factor Receptor 5 (FGFR5) Is a Co-Receptor for FGFR1 That Is up-Regulated in Beta-Cells by Cytokine-Induced Inflammation. *J. Biol. Chem.* **2018**, *293*, 17218−17228.

(31) Lambert, T. J. FPbase: A Community-Editable Fluorescent Protein Database. *Nat. Methods.* **2019**, *16*, 277−278.

(32) Patel, B. N.; Mackness, M. I.; Connock, M. J. Peroxisomal Localization of Glucose-6-Phosphate Dehydrogenase and Pyrophosphate-Stimulated Dihydroxyacetone-Phosphate Acyltransferase in Mouse Kidney. *Biochem. J.* **1987**, *244*, 443−448.

(33) Frederiks, W. M.; Vreeling-sindela, H.; Van Noorden, C. J. F. Loss of Peroxisomes Causes Oxygen Insensitivity of the Histochemical Assay of Glucose-6-Phosphate Dehydrogenase Activity to Detect Cancer Cells. *J. Histochem. Cytochem.* **2007**, *55*, 175−181.

(34) Antonenkov, V. D. Dehydrogenases of the Pentose Phosphate Pathway in Rat Liver Peroxisomes. *Eur. J. Biochem.* **1989**, *183*, 75−82.

(35) Goedhart, J.; Von Stetten, D.; Noirclerc-Savoye, M.; Lelimousin, M.; Joosen, L.; Hink, M. A.; Van Weeren, L.; Gadella, T. W. J.; Royant, A. Structure-Guided Evolution of Cyan Fluorescent Proteins towards a Quantum Yield of 93%. *Nat. Commun.* **2012**, *3*, No. 751.

(36) Cunningham, A. D.; Colavin, A.; Huang, K. C.; Mochly-Rosen, D. Coupling between Protein Stability and Catalytic Activity Determines Pathogenicity of G6PD Variants. *Cell Rep.* **2017**, *18*, 2592−2599.

(37) Dzyakanchuk, A. A.; Balázs, Z.; Nashev, L. G.; Amrein, K. E.; Odermatt, A. 11*β*-Hydroxysteroid Dehydrogenase 1 Reductase Activity Is Dependent on a High Ratio of NADPH/NADP+ and Is Stimulated by Extracellular Glucose. *Mol. Cell. Endocrinol.* **2009**, *301*, 137−141.

(38) Geisbrecht, B. V.; Gould, S. J. The Human PICD Gene Encodes a Cytoplasmic and Peroxisomal NADP+-Dependent Isocitrate Dehydrogenase. *J. Biol. Chem.* **1999**, *274*, 30527−30533.

(39) Crameri, F. *Scientific Colour-Maps*; Zenodo, 2018; Vol. *10*.

(40) Zhang, G. F.; Jensen, M. V.; Gray, S. M.; El, K.; Wang, Y.; Lu, D.; Becker, T. C.; Campbell, J. E.; Newgard, C. B. Reductive TCA Cycle Metabolism Fuels Glutamine- and Glucose-Stimulated Insulin Secretion. *Cell Metab.* **2021**, *33*, 804−817.

(41) Smith, H. Q.; Li, C.; Stanley, C. A.; Smith, T. J. Glutamate Dehydrogenase, a Complex Enzyme at a Crucial Metabolic Branch Point. *Neurochem. Res.* **2019**, *44*, 117−132.

(42) Chareyron, I.; Wall, C.; Thevenet, J.; Santo-Domingo, J.; Wiederkehr, A. Cellular Stress Is a Prerequisite for Glucose-Induced Mitochondrial Matrix Alkalinization in Pancreatic beta-Cells. *Mol. Cell. Endocrinol.* **2019**, *481*, 71−83.

(43) Batenburg, J. J.; Olson, M. S. Regulation of Pyruvate Dehydrogenase by Fatty Acid in Isolated Rat Liver Mitochondria*. *J. Biol. Chem.* **1976**, *251*, 1364−1370.

(44) Rydström, J. Site-Specific Inhibitors of Mitochondrial Nicotinamide-Nucleotide Transhydrogenase. *Eur. J. Biochem.* **1972**, *31*, 496−504.

(45) Orij, R.; Postmus, J.; Ter Beek, A.; Brul, S.; Smits, G. J. In Vivo Measurement of Cytosolic and Mitochondrial PH Using a PH-Sensitive GFP Derivative in *Saccharomyces cerevisiae* Reveals a Relation between Intracellular PH and Growth. *Microbiology* **2009**, *155*, 268−278.

(46) Wu, M. M.; Llopis, J.; Adams, S.; Mccaffery, J. M.; Kulomaa, M. S.; Machen, T. E.; Moore, H. P. H.; Tsien, R. Y. Organelle PH Studies Using Targeted Avidin and Fluorescein − Biotin. *Chem. Biol.* **2000**, *7*, 197−209.

(47) Llopis, J.; Mccaffery, J. M.; Miyawaki, A.; Farquhar, M. G.; Tsien, R. Y. Measurement of Cytosolic, Mitochondrial, and Golgi PH in Single Living Cells with Green Fluorescent Proteins. *Proc. Natl. Acad. Sci. U.S.A.* **1998**, *95*, 6803−6808.

(48) Poburko, D.; Santo-domingo, J.; Demaurex, N. Dynamic Regulation of the Mitochondrial Proton Gradient during Cytosolic Calcium Elevations. *J. Biol. Chem.* **2011**, *286*, 11672−11684.

(49) Jankowski, A.; Kim, J. H.; Collins, R. F.; Daneman, R.; Walton, P.; Grinstein, S. In Situ Measurements of the PH of Mammalian Peroxisomes Using the Fluorescent Protein PHluorin. *J. Biol. Chem.* **2001**, *276*, 48748−48763.

(50) Goedhart, J.; Von Stetten, D.; Noirclerc-savoye, M.; Lelimousin, M.; Joosen, L.; Hink, M. A.; Van Weeren, L.; Gadella, T. W. J., Jr; Royant, A. Structure-Guided Evolution of Cyan Fluorescent Proteins towards a Quantum Yield of 93%. *Nat. Commun.* **2012**, *3*, No. 751.

(51) Tischler, M. E.; Friedrichs, D.; Coll, K.; Williamson, J. R. Pyridine Nucleotide Distributions and Enzyme Mass Action Ratios in Hepatocytes from Fed and Starved Rats. *Arch. Biochem. Biophys.* **1977**, *184*, 222−236.

(52) Veech, R. L.; Eggleston, L. V.; Krebs, H. A. The Redox State of Free Nicotinamide-Adenine Dinucleotide Phosphate in the Cytoplasm of Rat Liver. *Biochem. J* **1969**, *115*, 609−619.

(53) Hedeskov, C. J.; Capito, K.; Thams, P. Cytosolic Ratios of Free INADPHI/INADP+I and INADHI/INAD+I in Mouse Pancreatic Islets, and Nutrient-Induced Insulin Secretion. *Biochem. J* **1987**, *161*−167.

(54) Smolková, K.; Ježek, P. The Role of Mitochondrial NADPH-Dependent Isocitrate Dehydrogenase in Cancer Cells. *Int. J. Cell Biol.* **2012**, *2012*, No. 273947.

(55) Bellomo, G.; Vairetti, M.; Stivala, L.; Mirabelli, F.; Richelmi, P.; Orrenius, S. Demonstration of Nuclear Compartmentalization of

Glutathione in Hepatocytes. *Proc. Natl. Acad. Sci. U.S.A.* **1992**, *89*, 4412−4416.

(56) Pallardó, F. V.; Markovic, J.; García, J. L.; Viña, J. Role of Nuclear Glutathione as a Key Regulator of Cell Proliferation. *Mol. Aspects Med.* **2009**, *30*, 77−85.

(57) Chang, H. H.; Bennett, A. M.; Cameron, W. D.; Floro, E.; Au, A.; McFaul, C. M.; Yip, C. M.; Rocheleau, J. V. Targeting Apollo-NADP+ to Image NADPH Generation in Pancreatic Beta-Cell Organelles *bioRxiv* 2022, DOI: 10.1101/2022.04.27.489691.